Combined-cycle gas turbine power plant integration with cascaded latent heat thermal storage for fast dynamic responses

Decai Li [a], Yukun Hu [b], Dacheng Li [c], Jihong Wang [a,d*]

[a] School of Engineering, University of Warwick, Coventry, CV4 7AL, UK
[b] School of Management, Cranfield University, Bedford, MK43 0AL, UK
[c] Institute of Process Engineering, Chinese Academy of Sciences, Beijing, 100190, P.R. China
[d] Huazhong University of Science and Technology, Wuhan, P.R.China

Abstract

The combined-cycle gas turbine (CCGT) power plants are often required to provide the essential fast grid balance service between the load demand and power supply with the increase of the intermittent power generation from renewable energy sources. It is extremely challenging to ensure CCGT power plants operating flexibly and also maintaining its efficiency at the same time. This paper presents the feasibility study of a CCGT power plant combined with the cascaded latent heat storage (CLHS) for plant flexible operation. A 420 MW CCGT power plant and a CLHS dynamic models are developed in Aspen Plus based on a novel modelling approach. The plant start-up processes are studied, and large amount of thermal energy can be accumulated by CLHS during the start-up. For load-following operation, extensive dynamic simulation study is conducted and the simulation results show that the extracted exhaust gas can be used for thermal energy storage charging, and the stored heat can be discharged to produce high temperature and high pressure steam fed to the steam turbine. Besides, the stored heat can also be used to maintain the heat recovery steam generator (HRSG) under warm condition to reduce plant restart-up time. The simulation results demonstrate that the integration of CLHS with CCGT power plant is feasible during the start-up, load-following and standstill operations.

Keywords: combined-cycle gas turbine; cascaded latent heat storage; flexible operation; dynamic modelling; Aspen Plus

Highlights:

- Dynamic modelling of combined-cycle gas turbine power plant with thermal storage.
- Cascaded latent heat storage integration strategies to plant operation processes.
- Complete system dynamic simulations of the plant with cascaded latent heat storage.
- Quantified analysis of stored and released thermal energy for different strategies.

1. Introduction

Combined-cycle power generation technology has been developed and served as an effective means for base load supply worldwide since the 1960s due to its inherent advantages in high efficiency and operational flexibility [1]. Although the technology in design and operation of combined-cycle gas

*Corresponding author at: School of Engineering, University of Warwick, UK.
E-mail addresses: jihong.wang@warwick.ac.uk (Prof. J. Wang)

turbine (CCGT) plants is now widely available, CCGT plants face new technical challenges nowadays in terms of efficient flexible operation to support the integration of intermittent renewable energy. Over the past 10 years, the capacity of intermittent renewable energy has increased dramatically, which has a significant impact on maintaining the balancing of the power generation and demand. This forces CCGT power plants into a role change: from base load supply to fast response operating services. This has led to a series of potential issues, such as low plant operation energy efficiency, low load factors, and potentially shortened plant life time. To address those issues, this paper investigates a new potential solution – to integrate the plant with thermal storage to create an energy buffer for fast energy dispatch to support plant flexible operation.

In recent years, the study on flexible plant operation has started being given important consideration and several studies the start-up process of CCGT power plants are reported [2, 3]. Those paper focused on optimizing the start-up process, but the dynamic performance of CCGT power plants operating flexibly under different load conditions have not been extensively studied. With the increase of renewable generation, the impact of passive operation of power plants during load changes has received more attention. The flexible operation of CCGT power plants could enhance the stability of the grid dynamics and maximise short-term high profits, but it will lead to a significant reduction in the lifetime of the power plant equipment [4]. Therefore, many solutions have been proposed to enhance the flexible output of the power plant without compromising its residual life, such as integrated with energy storage systems. CCGT power plants integrated with electrical energy storage was proposed to compensate the intermittent solar power generation [5]. Various thermal power plants integrated with thermal energy storage (TES) were proposed to align power or heat generation with the load demand, including solar thermal power plants [6-8], combined heat and power (CHP) plants [9], and conventional fossil fuel power plants [10, 11]. One study is reported that CCGT power plant integrated with a CO_2 capture unit to achieve load-following operations [12]; oxy-fuel power plant integrated with air separation unit (ASU) to help respond load changes through peak and off-peak operations [13, 14].

Realisation of dynamic modelling of CCGT power plant processes is still a challenge task. Recently, several studies on dynamic modelling of different types of power plants have been published. Hübel et al. developed a coal-fired power plant model for start-up optimisation [15]. Zhao et al. developed a supercritical coal-fired power plant model using the GSE software to explore strategies of improving operational flexibility [16]. A dynamic model of adiabatic compressed air energy storage plant with packed bed thermal storage was presented in [17]. However, the work on the development of dynamic models for CCGT power plants is very limited, besides a combined-cycle power plant was modelled using software Apros [1] and three different dynamic models of the same CCGT power plant presented in [4].

In addition, with the maturity of commercial software for process simulations, various process simulators such as Aspen Plus® are available and have been widely employed for process simulation purposes by industrial entities since the late 1990s [18-21]. However, all of these studies are based on steady state models. To assess the efficiently flexible plant operation, it is essential to present the dynamic behaviour of variable load demand. Therefore, to derive the CCGT power plant and CLHS dynamic models is the core of the study. This paper will propose a novel modelling approach to address the limitation and capture the main dynamic behaviour of the simulated system in Aspen Plus by incorporated an external dynamic model.

From the known literature, it is noticed that CCGT power plant integration with cascaded latent heat storage (CLHS) for flexible plant operation has not been reported. The scope of the paper is thus concerned with the flexible operations of the CCGT power plant through integration of CLHS to the plant process. A novel modelling approach is developed and used for study of the integrated dynamic behaviours. This approach incorporates an "explicit difference method" based CLHS models into the "sequential modular strategy" based CCGT power plant model in Aspen Plus, while further taking into account the charging and discharging processes within the different phase change material (PCM) layers. A 420 MW triple-pressure CCGT power plant model is developed to investigate its potential integration strategies with CLHS which stores thermal energy during the start-up processes; to operate flexibly during the load-following operation; and to keep heat recovery steam generator (HRSG) warm during the standstill period.

This paper is organised as follows: Section 2 brief describes the CCGT power plant and its operating conditions; Section 3 presents the mathematical models of the gas turbine, HRSG, steam turbine, and CLHS; Section 4 offers results and discussion of the proposed integration strategies; finally, in Section 5 conclusions in relation to this overall study are drawn, with clearly outlined suggestions for future exploitation.

2. Power plant description

A CCGT power plant generally consists of the gas turbine, HRSG and steam turbines, as shown in Figure 1. Air is compressed via a compressor and is mixed with natural gas (NG) in the combustion chamber for combustion, then hot combustion gas expands in the gas turbine, which forms a Brayton cycle; the heat from the gas turbine exhaust is used to generate steam for steam turbine, that is, the heat passes through the HRSG to heat the water flow, which formulates a Rankine cycle. In this way, the CCGT power plant can achieve a much higher thermal efficiency than a single cycle gas turbine power plant, because the waste heat from the gas turbine exhaust is recovered via the HRSG which is then used by the steam turbines for electricity generation.

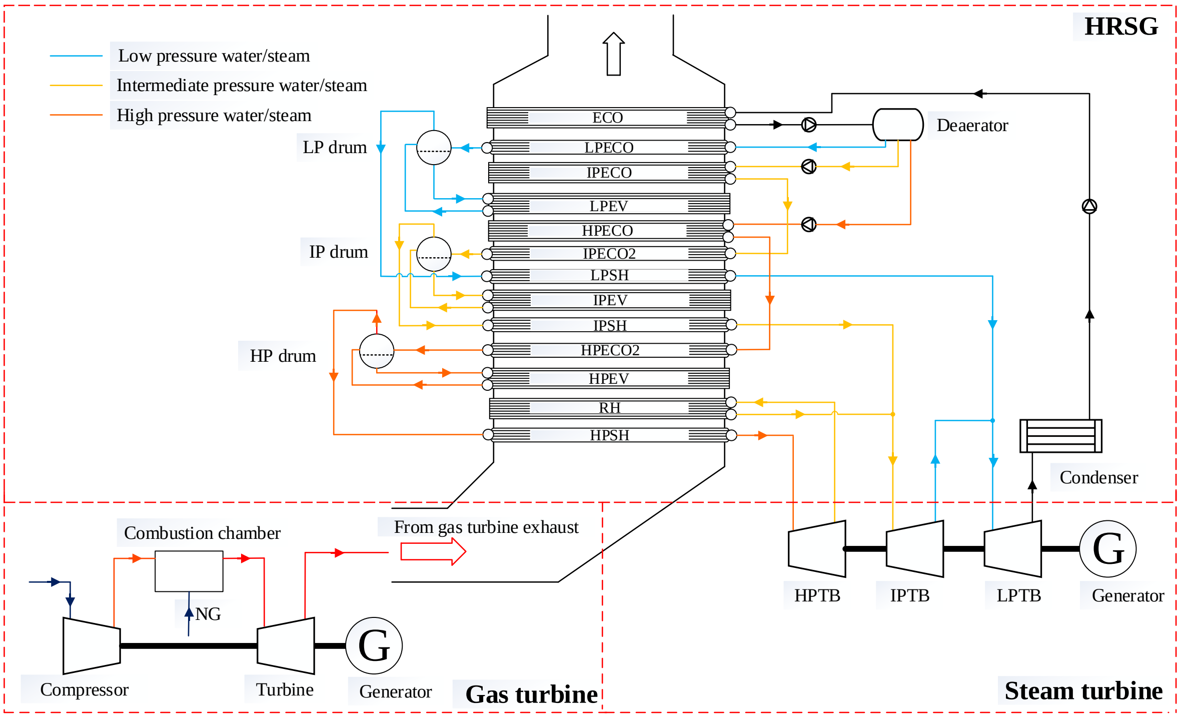

Figure 1: The schematic of a 420 MW CCGT power plant.

A 420 MW CCGT power plant is sued for this study and the plant which has three pressure levels steam drums (HP, IP, and LP) [22], as shown in Figure 1. The CCGT power plant rated state are listed in Table 1.

Table 1: Parameters of developed CCGT power plant.

Parameter	Value
Gas turbine power	285 MW
Steam turbine power	135 MW
Exhaust gas mass flow rate	685 $kg \cdot s^{-1}$
Exhaust gas temperature	846 K
Feed water flow rate	108 $kg \cdot s^{-1}$
High pressure steam turbine inlet pressure	140 bar
Intermediate pressure steam turbine inlet pressure	25 bar
Low pressure steam turbine inlet pressure	6 bar
Low pressure steam turbine outlet pressure	0.05 bar

3. Dynamic modelling of CCGT power plant and thermal energy storage

Aspen Plus was used to develop the dynamic model of the CCGT power plant. The PR-BM property method [23] was chosen for the physical property calculation of the gas cycle, and STEAMNBS property method [24] was chosen for the physical property calculation of the water-steam cycle calculation. To implement the dynamic modelling, the built-in ‘calculator’ block was used to define time-dependent variables. The sequential model approach is used for simulation of the whole system. It takes modules as basic computational unit and through sequential calculation of each modules to solve the model. The sequential model approach is widely used for the process modelling, since it improves the accuracy of the model and reduces the difficulty of system modelling and solving.

3.1 Gas turbine section modelling

The gas turbine section consists of three components: a compressor, a combustion chamber, and a turbine. For the compressor, it was modelled as a polytropic compression process that gives a more accurate calculation of the power required for multi-state compressor, and its power consumption can be calculated by Eq. (1) [22]:

$$W_{in,\,ideal} = \left(\frac{\gamma}{\gamma - 1}\right) P_{in} V_{in} \left[\left(\frac{P_{out}}{P_{in}}\right)^{(\gamma-1)/\gamma} - 1\right], \quad (1)$$

$$W_{in} = \frac{W_{in,\,ideal}}{\eta_c}, \quad (2)$$

where, $W_{in,\,ideal}$ is the power consumption under ideal polytropic condition, γ is the specific heat ratio, P_{in} is the inlet pressure, V_{in} is the inlet volume, P_{out} is the outlet pressure, W_{in} is the real power consumption, and η_c is the compressor polytropic efficiency.

The mechanical efficiency of the compressor used in the simulation is 0.985. The actual polytropic efficiency of compressor varies with mass flow rate and can be determined by Figure 2 [25]. The efficiency curve is formulated by using several high-order polynomial equations, in order to minimise errors. And then the ploytropic efficiency is incorporated into Aspen Plus by a FORTRAN subroutine, and updated each time-step based on the instant compressor mass flow rate.

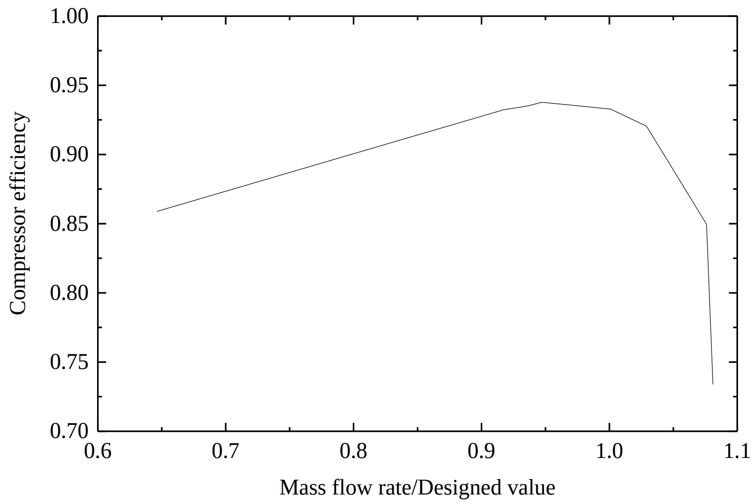

Figure 2: Compressor efficiency curve.

The temperature of the compressor outlet stream is given by:

$$T_{out} = \frac{T_{in}}{\eta_c}\left[\left(\frac{P_{out}}{P_{in}}\right)^{(\gamma-1)/\gamma} - 1\right] + T_{in}, \quad (3)$$

where, T_{out} is the outlet temperature, and T_{in} is the inlet temperature. The air composition used in modelling are given in Table 2.

Table 2: Air composition in molar fraction [26].

Components	Molar Fraction (%)
N_2	75.67
O_2	20.35
H_2O	3.03
CO_2	0.345
Others	0.915

The natural gas composition used in the modelling is given in Table 3. It consists of methane, ethane, propane, nitrogen, carbon dioxide, and other gases and the methane and ethane account make up more than 99% of the total volume [27]. Therefore, only two reactions are considered in the combustion process:

$$CH_4 + 2O_2 = CO_2 + 2H_2O\,, \tag{4}$$

$$C_2H_6 + \frac{7}{2}O_2 = 2CO_2 + 3H_2O\,. \tag{5}$$

Table 3: Nature gas composition in molar fraction.

Components	Molar Fraction (%)
CH_4	98.57
C_2H_6	0.82
N_2	0.6
CO_2	0.01

For the turbine, it was modelled as an isentropic process, and its output power is calculated by Eq. (6) [22]:

$$W_{out,\,ideal} = -\left(\frac{\gamma}{\gamma-1}\right)P_{in}V_{in}\left[\left(\frac{P_{out}}{P_{in}}\right)^{(\gamma-1)/\gamma} - 1\right], \tag{6}$$

$$W_{out} = \eta_t W_{out,\,ideal}\,, \tag{7}$$

where, $W_{out,\,ideal}$ is the turbine output power under ideal isentropic condition, W_{out} is the real turbine output power, and η_t is the isentropic efficiency.

The isentropic efficiency of the turbine is defined as [28]:

$$\eta_t = 0.91[1-0.3(1-\dot{n}_t)^2](\dot{n}_t / \dot{m}_t)(2-\dot{n}_t / \dot{m}_t) \tag{8}$$

where, $\dot{n}_t$ is the ratio of rotating speed to its designed value, and $\dot{m}_t$ is the ratio of mass flow rate to its designed value.

The temperature of the turbine outlet stream is given by:

$$T_{out} = T_{in} - \eta_t T_{in}\left[1-\left(\frac{P_{out}}{P_{in}}\right)^{(\gamma-1)/\gamma}\right]. \tag{9}$$

3.2 HRSG section modelling

The HRSG is modelled as a group of heat exchangers in this study. The exhaust gas from the gas turbine enters the HRSG, where the waste heat is recovered to produce steam at different pressure levels (HP, IP, and LP). The heat exchanger dynamic model was developed based on energy and mass balance equations.

The energy conservation equation is given by [29, 30]:

$$V\rho\frac{\partial h}{\partial t}+m\frac{\partial h}{\partial z}dz=Q+W\ , \tag{10}$$

and mass balance gives [3]:

$$\frac{\partial \rho}{\partial t}+\frac{\partial \rho v}{\partial z}=0 \tag{11}$$

The heat flux can be calculated by Eq. (12):

$$Q=UA\Delta T\ . \tag{12}$$

In order to capture the dynamics of the heat exchanger, the heat exchanger is discretized into several zones, as shown in Figure 3, each of which obey both energy and mass conservation equations [29].

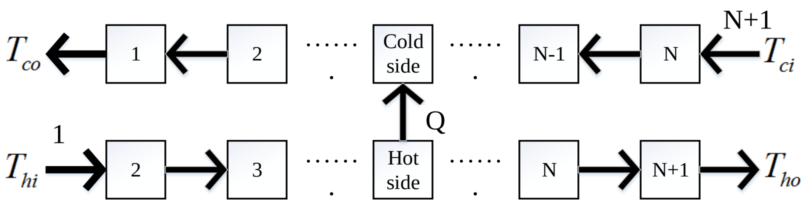

Figure 3: Cell model of the counter current heat exchanger.

The instantaneous temperature change of cold stream can be calculated by Eq. (13):

$$\frac{dT_{c,i}}{dt}=\frac{UA_i(T_{h,i+1}-T_{c,i})-m_c c_{p,ci}(T_{c,i}-T_{c,i+1})}{V_i\rho_{c,i}c_{p,ci}}\ . \tag{13}$$

Similarly, the instantaneous temperature change of hot stream can be calculated by Eq. (14):

$$\frac{dT_{h,i}}{dt}=\frac{-UA_i(T_{h,i}-T_{c,i-1})+m_h c_{p,hi}(T_{h,i-1}-T_{h,i})}{V_i\rho_{h,i}c_{p,hi}}\ . \tag{14}$$

In the model simulation, the thermodynamic properties (e.g. heat capacity and density) of the exhaust gas and water/steam are updated at every time-step based on the current temperature and pressure using Aspen Plus's thermodynamic database.

3.3 Steam turbine section modelling

Three levels of steam generated by the HRSG are used to spin the corresponding three steam turbines: high pressure turbine (HPTB), intermediate pressure turbine (IPTB), and low pressure turbine (LPTB). The development of the steam turbine models uses the same thermodynamic principles as the gas turbine model development, which is presented in Section 3.1. The actual isentropic efficiency of steam turbine varies with mass flow rate and can be determined by Figure 4 [31]. The nominal values of HPTB, IPTB, and LPTB used in the simulation were 0.88, 0.88 and 0.85, respectively.

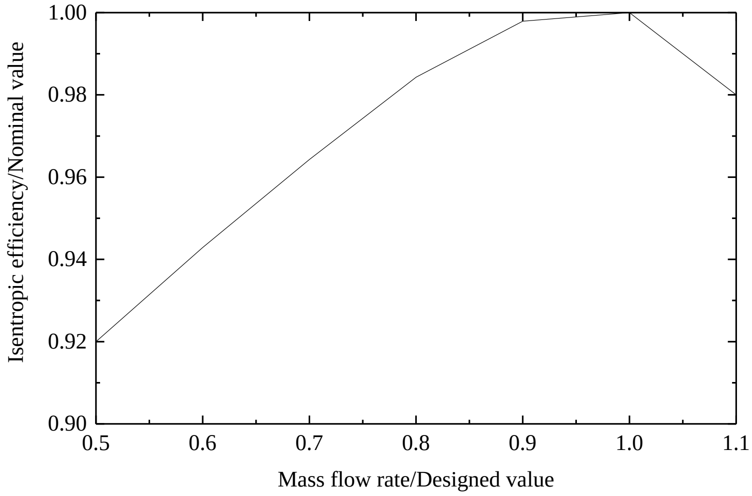

Figure 4: Steam turbine isentropic efficiency curve.

3.4 Cascaded latent heat storage (CLHS)

In the CLHS system, thermal energy is transferred to the storage media during charging, and is released in later discharging step. There are mainly three types of thermal energy storage: sensible heat storage, latent heat storage, and chemical heat storage [7]. The latent heat storage will be used for this study because its energy density is much higher than sensible heat storage [32, 33] and the cost is lower than chemical heat storage. Besides, heat transfer irreversibility of a latent heat storage system can be significantly reduced using cascaded phase change materials [7].

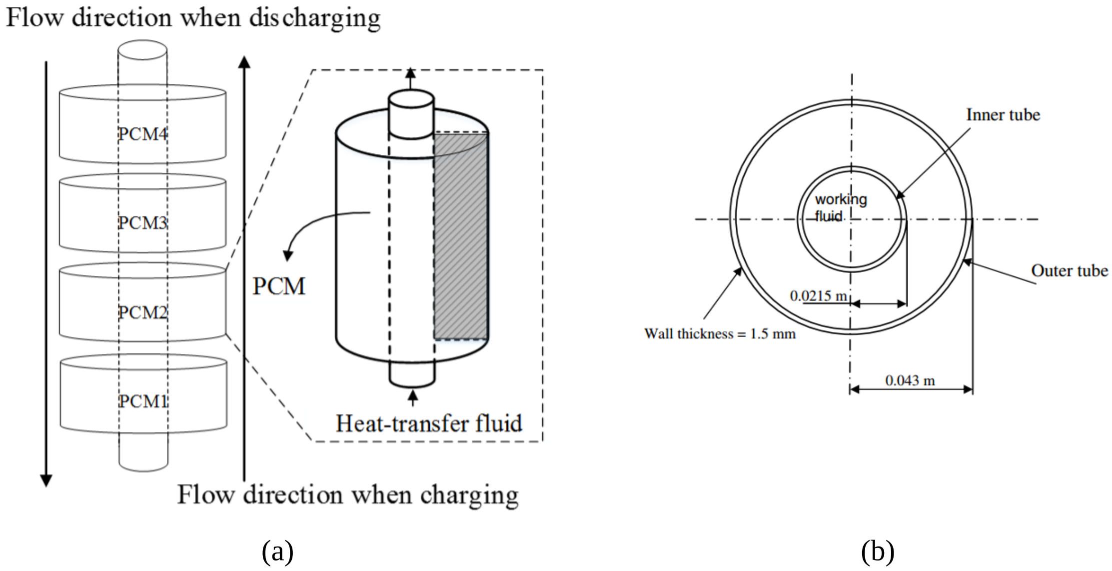

Figure 5: Structure of a signal CLHS set (a) and its sectional view (b) [34].

The designed CLHS system in this study consists of four PCM layers, which are NaCl&$CaCl_2$ (PCM1), $MgCl_2$&NaCl&KCl (PCM2), LiCl&LiOH (PCM3), $LiNO_3$&$NaNO_3$&KCl (PCM4). These PCM layers are arranged in the direction of charging flow as shown in Figure 5 (a) and their thermodynamic properties are listed in Table 4. The basic structure of the CLHS system consists of two vertical concentric tubes filled with four cascaded PCM layers in between [34], as shown in Figure 5 (a), with a radius of 0.0215 m for the inner tube and 0.043 m for the outer tube, a wall thickness of 0.0015 m, and a height of 20 m (5 m for each PCM layer), as shown in Figure 5 (b). The entire CLHS system consists of 5600 sets of such concentric tubes in parallel.

The consideration for such an arrangement is that heat is required to be quickly absorbed or released during the charging or discharging processes. The temperature difference decreases in the flow direction of the working fluid in a single PCM layer and results in a decrease in the heat transfer rate and thereby mediocre performance. The multiple PCM layers with different phase change temperature are cascaded in decreasing order of phase change temperature, so despite the decrease in the heat transfer fluid temperature the temperature difference can still be maintained constantly during charging [35]. For the discharging, the heat-transfer fluid flows in the opposite direction so that the PCM layers are arranged in ascending order of phase change temperature, thus maintaining the temperature difference between the PCM layers and the heat-transfer fluid.

At rated state, the temperature of gas turbine exhaust gas is 846 K, therefore the material PCM1 is chose whose melting temperature is 773 K. In this way, the outlet temperature of PCM1 will not exceed 773 K for the charging process. This guarantees the maximum temperature of PCM2 will be less than 773 K. Moreover, the PCMs have to operate around the melting point to ensure safety and without poisonous gas generated. For these reasons, the materials listed in Table 4 are selected for the proposed model.

Table 4: Thermophysical properties of PCMs [36].

Material	Composition, wt%	Melting temp., K	Latent heat, J/g	Specific heat, J/(g·K)	Density, g/cm^3	Conductivity, W/mK
PCM1	33 (NaCl) 67 ($CaCl_2$)	773	280	1	2.16	1.02
PCM2	63 ($MgCl_2$) 22.3 (NaCl) 14 (KCl)	658	461	0.96	2.25	0.95
PCM3	37 (LiCl) 63 (LiOH)	535	485	2.4	1.55	1.1
PCM4	55.4 ($LiNO_3$) 4.5 ($NaNO_3$) 40.1 (KCl)	433	266	1.4	2.21	1

In the CLHS system, the heat transfer process is coupled with heat convection and heat conduction. Heat transfer fluid transfers heat to the inner tube by means of heat convection. For the heat transfer from the inner tube to the PCM and the heat diffusion in the PCM, the heat transfer is by means of heat conduction. The heat loss through the outer tube of the CLHS system is assumed negligible. Figure 6 shows a portion of a three-dimensional heat conduction grid.

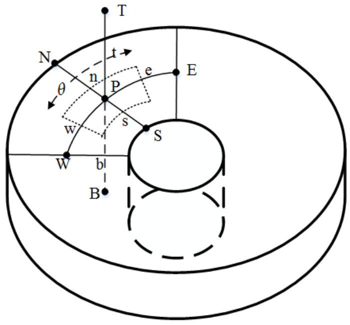

Figure 6: Three-dimensional heat conduction.

In a cylindrical-coordinate system, the three-dimensional heat conduction equation for the point *P* in the Figure 6 is given by [37]:

$$\rho c_p \frac{\partial T_P}{\partial t} = \frac{1}{r}\frac{\partial}{\partial r}(rk\frac{\partial T}{\partial r}) + \frac{1}{r}\frac{\partial}{\partial \theta}(\frac{k}{r}\frac{\partial T}{\partial \theta}) + \frac{\partial}{\partial z}(k\frac{\partial T}{\partial z}), \tag{15}$$

where, subscript *P* denotes the point *P* shown in Figure 6.

Due to the cylinder is symmetrical, the unique temperature in θ direction is assumed. Therefore, the heat conduction equation in the cylinder is given by [38]:

$$\rho c_p \frac{\partial T_P}{\partial t} = \frac{1}{r}\frac{\partial}{\partial r}(rk\frac{\partial T}{\partial r}) + \frac{\partial}{\partial z}(k\frac{\partial T}{\partial z}). \tag{16}$$

The discretization equation is obtained by integrating the differential equations in the control volume over the time interval from t to $t+\Delta t$. The discretized equation is shown as follows [37]:

$$\begin{aligned} a_P T_P = {} & a_N[fT_N - (1-f)T_N^0] + a_S[fT_S - (1-f)T_S^0] + a_T[fT_T - (1-f)T_T^0] + \\ & a_B[fT_B - (1-f)T_B^0] + [a_P^0 - (1-f)a_N - (1-f)a_S - (1-f)a_T - (1-f)a_B]T_P^0, \end{aligned} \tag{17}$$

where, $a_N = \dfrac{kr_n\Delta\theta\Delta z}{(\delta r)_n}$, $a_S = \dfrac{kr_s\Delta\theta\Delta z}{(\delta r)_s}$, $a_T = \dfrac{k0.5(r_n + r_s)\Delta\theta\Delta r}{(\delta z)_t}$, $a_B = \dfrac{k0.5(r_n + r_s)\Delta\theta\Delta r}{(\delta z)_b}$, $a_P^0 = \dfrac{\rho c\Delta V}{\Delta t}$, and $a_P = fa_N + fa_S + fa_T + fa_T + a_P^0$. Subscripts *N* and *n* are north side points, *S* and *s* are south side points, *T* and *t* are top side points, and *B* and *b* are bottom side points, as shown in Figure 6.

The ΔV is the volume of the control volume, which is given by:

$$\Delta V = 0.5(r_n + r_s)\Delta\theta\Delta r\Delta z. \tag{18}$$

There are three methods available for solving the discretised partial differential equation that depends on the value of the weighting factor (f). In particular, $f = 0$ leads to the explicit scheme, $f = 0.5$ to the Crank-Nicolson scheme, and $f = 1$ to the fully implicit scheme. The explicit scheme is used to discretize the differential equation in this study, as follows:

$$a_P T_P = a_N T_N^0 + a_S T_S^0 + a_T T_T^0 + a_B T_B^0 + (a_P^0 - a_N - a_S - a_T - a_B)T_P^0. \tag{19}$$

This means that T_P is not related to other unknown temperatures such as T_N, T_S, T_T and T_B, but it is explicitly related to the known temperatures T_N^0, T_S^0, T_T^0 and T_B^0. The main advantage of the explicit scheme is that it can solve partial differential equations non-iteratively by direct calculation. However, for the explicit scheme, the time step (Δt) has to be small enough to maintain the simulation result accuracy and the time step in this study is set to 0.001s.

However, during the phase change, the temperature of the PCM is maintained at the melting temperature [39]. Therefore, the above equations are only used for calculations under pure solid and liquid conditions. To over the melting process, the following equation is introduced to calculate the enthalpy change during PCM melting [7, 32, 38]:

$$\rho \frac{\partial H_P}{\partial t} = \frac{1}{r}\frac{\partial}{\partial r}(rk\frac{\partial T}{\partial r}) + \frac{\partial}{\partial z}(k\frac{\partial T}{\partial z}) . \tag{20}$$

The discretization equation is given by:

$$a_P{}'(H_P - H_P^0) = a_N T_N^0 + a_S T_S^0 + a_T T_T^0 + a_B T_B^0 + (-a_N - a_S - a_T - a_B) T_P^0 , \tag{21}$$

where, $a_P{}' = \frac{\rho \Delta V}{\Delta t}$. The H_P^0 is the known enthalpy (old enthalpy), and the discretization method is also explicit scheme. Due to the outer tube is assumed adiabatic, there is no heat conduction on the boundary. Thus a_T is set as 0 for the topmost side of PCM, a_B is set as 0 for the bottommost side of PCM, and a_N is set as 0 for the outermost side of PCM.

The CLHS model is developed based on the above discretized equations and incorporated into Aspen Plus model through an external FORTRAN subroutine. The thermodynamic properties of the working fluid are calculated by the Aspen Plus's thermodynamic database, while the properties of the PCMs are using the data from literature which is listed in Table 4. The validation of the CCGT power plant and latent heat storage model is presented in the previous publication [31].

4. Results and discussion

This section presents the integration strategies of CCGT power plant with CLHS during the start-up, load-following operation, and standby, respectively. In particular, the start-up procedure is studied, and the idea of energy storage during plant start-up is proposed. The paper examines how the integration of CLHS impact on the performance of the plant regarding to the output power and CLHS charging or discharging processes. The plant output power can be regulated through variation of CLHS charging and discharging processes. The stored thermal energy can also be used to keep HRSG warm during plant standby so as to restart faster.

4.1 CLHS integration strategy during the plant start-up

In practice, although the gas turbine can start-up from cold state to nominal load condition within 20 minutes, it takes up to 170 minutes for the HRSG to reach its nominal load, depending on the initial temperature state of start-up, that is, hot, warm or cold [40]. This is due to the high thermal stress of the HRSG section, which is caused by the temperature gradient in metal. In order to reduce thermal stress of the HRSG, a bypass damper is used to control the gas flow to the HRSG [41]. Therefore, only a small part of the exhaust gas passes through the HRSG at the start-up, and most of the exhaust gas is directly discharged into the atmosphere, resulting in energy loss. As described in [42], approximately 75% of the exhaust gas (513 kg/s in this study) from the gas turbine is discharged into the atmosphere for 25 minutes during the plant start-up. However, this waste energy is potential to be captured by the CLHS, as shown in Figure 7. The 75% of exhaust gas may first pass through the CLHS before discharging into atmosphere, and the other 25% of exhaust gas flows into HRSG, during the plant start-up process. A filter is needed to remove the corrosive gases of the exhaust gas, as shown in Figure 7, and the gas pressure of CLHS outlet is assumed to be the same as the atmosphere. In this way, waste heat in the exhaust gas can be captured by the PCM layers in the CLHS.

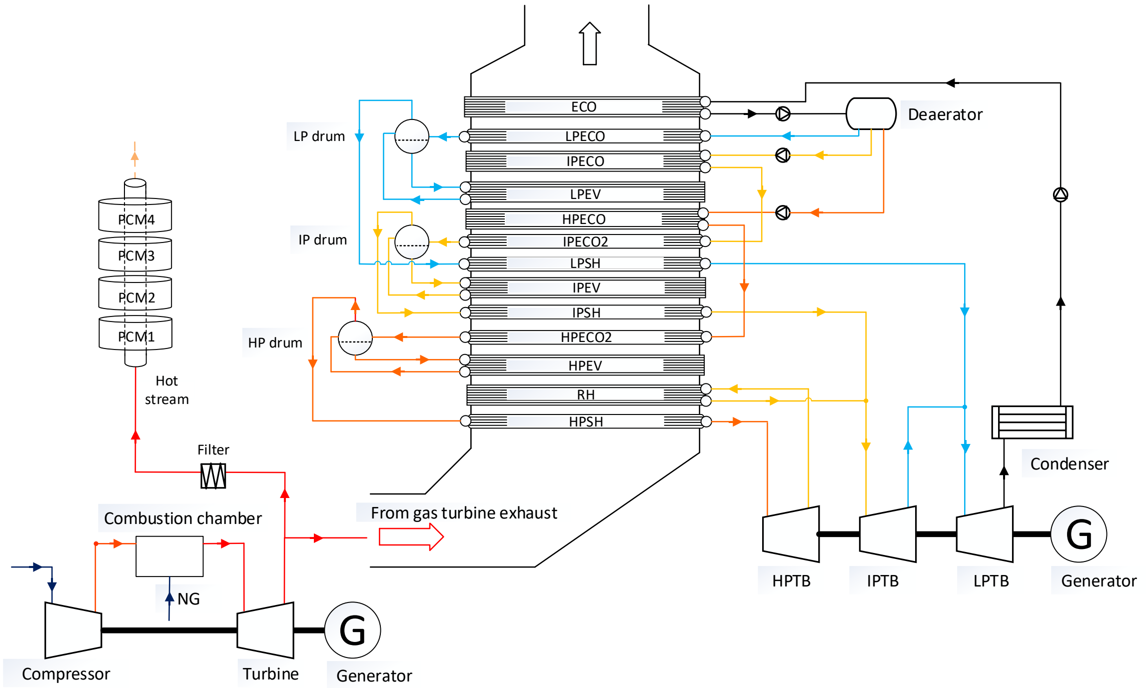

Figure 7: CLHS integration strategy for charging during plant start-up.

For PCM layers filled at the same height in the CLHS system, it can be assumed that they have the same temperature distribution due to their parallel structure [33]. Then the study of the entire CLHS system can be simplified as a study of one set of concentric tubes (Figure 5 (a)). In order to establish a reasonable initial temperature distribution of the PCM layers such that a phase change process occurs in the simulation, a temperature below the phase change point of each PCM is used to start up the CLHS, as listed in Table 5; when the local temperature reaches the phase transition point, the temperature distribution of each PCM at that time is its initial temperature distribution, as shown in Figure 8. The figure presents the temperature distribution of the shaded area in the Figure 5 (a). For each PCM layer, the phase change temperature is reached first in the lower left corner as expected. The axial temperature distribution coincides with the exhaust gas in the inner tube, while the radial temperature distribution also follows the heat conduction from the inside to the outside of the PCM.

Table 5: Parameter setting used to establish initial temperature distribution.

Layer	Start-up temp., K	Phase change temp., K	Initial temperature distribution
PCM4	387.7	433	Figure 8 (a)
PCM3	502	535	Figure 8 (b)
PCM2	596	686	Figure 8 (c)
PCM1	697	773	Figure 8 (d)

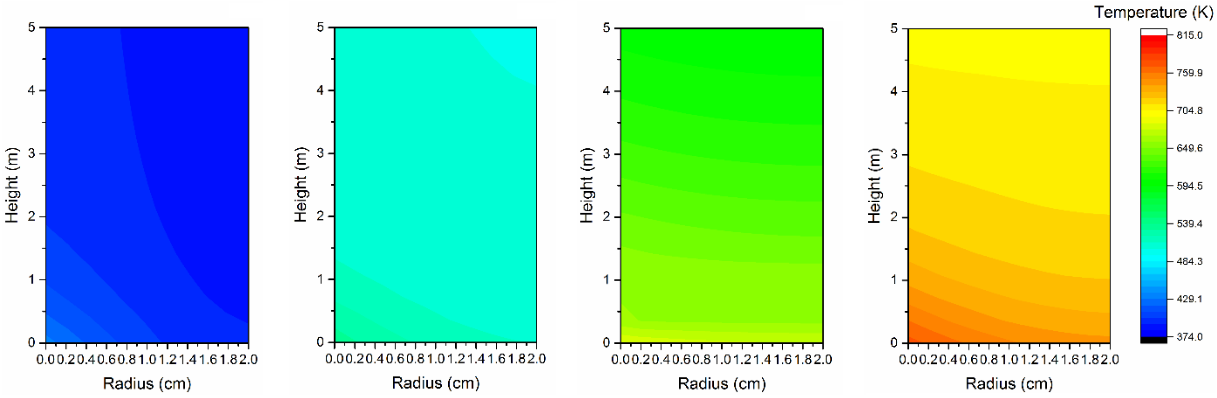

(a) PCM4 (b) PCM3 (c) PCM2 (d) PCM1

Figure 8: Initial temperatures distribution of different PCM layers.

After 1500 seconds of simulated charging process, waste heat in the exhaust gas is further diffused and stored in the PCMs. The lowest local temperature of each PCM layer reaches the phase transition point, and the temperature in the region where the local temperature is higher than the phase change point continues to increase after undergoing the phase change process. The updated temperature distribution of different PCM layers are shown in Figure 9. The plotted temperature is the right side of the concentric tubes (see Figure 5 (a)) and the gas flows from bottom to top, therefore, the heat diffuses from left side to right side, and from bottom side to top side as well.

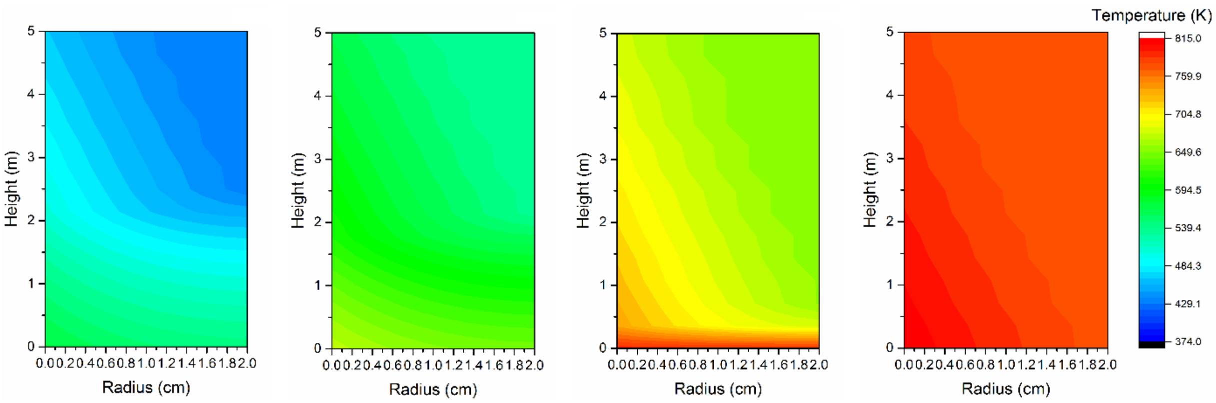

(a) PCM4 (b) PCM3 (c) PCM2 (d) PCM1

Figure 9: Temperature distribution of different PCM layers at the end of charging in the start-up operation.

The stored thermal energy ($Q_{storage}$) can be calculated by [7]:

$$Q_{storage} = M_{PCM}[\Delta T \cdot c_p + L], \qquad (22)$$

where, M_{PCM} is the mass of PCM, ΔT is the temperature change, c_p is the heat capacity, and L is the latent heat. According to the calculation, a total of 327 GJ heat is stored in the CLHS system in the 1500 seconds, and from left to right each PCM layer stores heat of 88 GJ, 101 GJ, 83 GJ, and 55 GJ, respectively.

4.2 CLHS integration strategy during load-following operation

In addition to avoiding the energy loss of the exhaust gas during the start-up process, the real-time output power of the CCGT power plant can be regulated within a certain range by the CLHS charging and discharging processes. The response speed of CCGT power plant is mainly limited by the water-steam cycle, therefore, this section focuses on the utilization strategies of thermal storage in water-steam cycle. During off-peak time, part of the high-temperature exhaust gas is extracted from the gas turbine as a heat source for CLHS charging (same as the layout shown in Figure 7). As the result, the power generated by the steam turbines will be reduced, but the gas turbine section is still operating under the rated load condition. The minimum steam turbine power is 66 MW when 363 kg/s exhaust gas by pass to the CLHS for thermal storage. On the contrary, during peak time, part of the feed water from the deaerator flows into the CLHS, undergoing the reverse process of charging, it evaporates into high temperature steam, and then leaves CLHS as superheated steam, as shown in Figure 10. The maximum steam turbine output power increases to 143 MW. In order to produce dry steam for steam turbine, a separator is needed to separate water droplets from steam. Finally, the stored thermal energy is released from the CLHS to the feed water, thereby increasing the power output of the steam turbines.

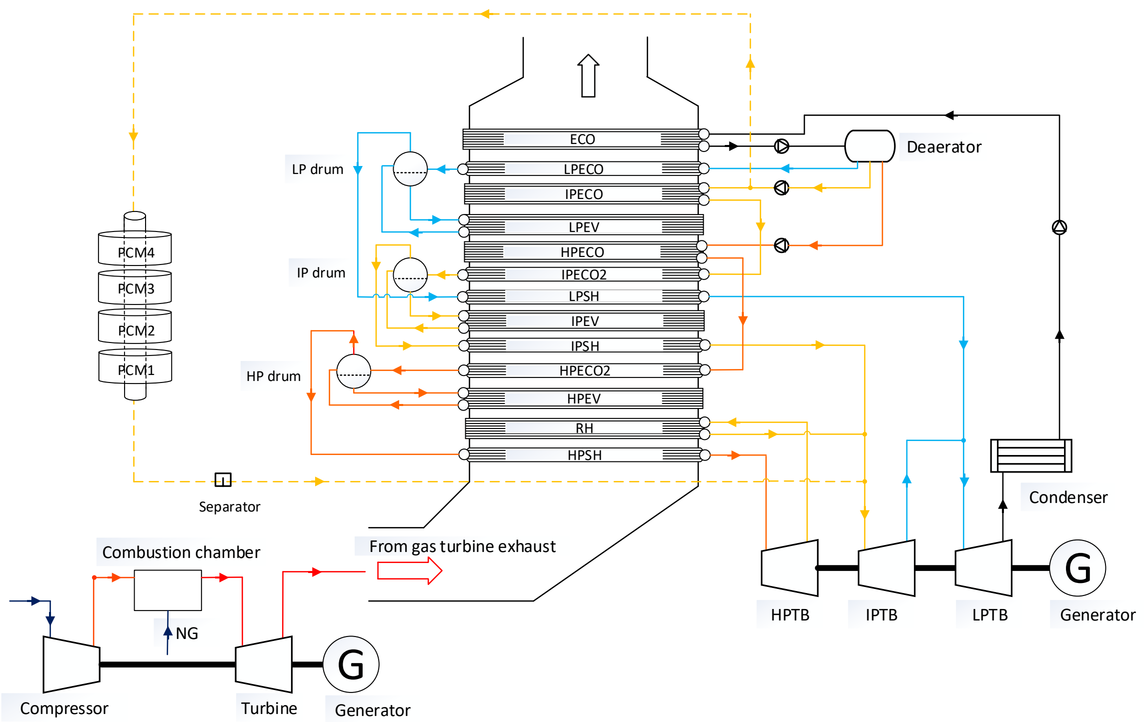

Figure 10: CLHS integration strategy for discharging during load-following operation.

The simulated discharging process is as follows. At beginning, the power plant operates at the nominal load condition, and the total output power is 420 MW, in which 285 MW is from the gas turbine and 135 MW is from the steam turbines. Figure 11 shows the designed load demand dynamics. At the 300th second, the load demand was reduced from 420 MW to 408 MW. After 1800 seconds, the load demand returned to 420 MW. At the 2800th second, the load demand increased again from 420 MW to 428 MW and lasted 1200 seconds. During this period, the gas turbine has been operating under rated conditions with an output power of 285 MW. As a result, the real-time power output of the power plant is determined by the steam turbines. It should be pointed out that the initial temperature distribution of the CLHS layers used for the load-following operation simulation is the same as the initial temperature distribution (Figure 8) in the start-up operation simulation.

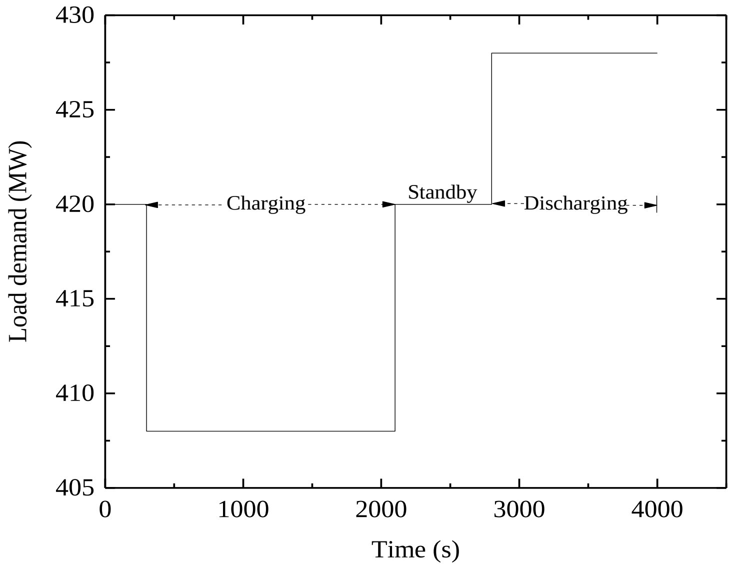

Figure 11: The desired load demand dynamics during load-following operation.

4.2.1 CLHS charging process

To meeting the load demand reduction from 420 MW to 408 MW, correspondingly the steam turbine output power was reduced from 135 MW to 123 MW, 60 kg/s of exhaust gas was extracted from the gas turbine outlet and sent to the CLHS. This is under charging conditions, so the extracted gas also flows from the bottom of the CLHS to its top, which is the direction along the PCM melting point in decreasing order. Figure 12 shows the temperature distribution of different PCM layers at the end of charging in the load-following operation (time = 2160s). Compared to the temperature distribution of different PCM layers in the start-up operation (Figure 9), the radial temperature difference of each PCM layer is significantly reduced. This is because the charging time in the load-following operation is longer than that in the start-up operation. Thus, the thermal diffusion in the PCM is more fully.

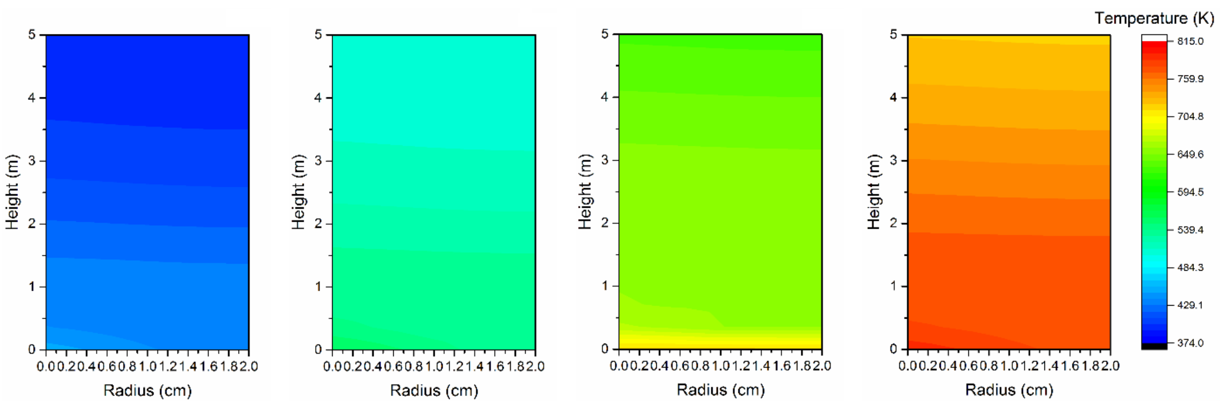

(a) PCM4 (b) PCM3 (c) PCM2 (d) PCM1

Figure 12: Temperature distribution of different PCM layers at the end of charging in the load-following operation.

4.2.2 CLHS standby process

After charging, the power demand returned to 420 MW, correspondingly the steam turbine output power returned to 135 MW. Followed by a nominal power demand of 700 seconds, the CLHS was on standby, i.e. neither charging nor discharging during this period. Figure 13 shows the temperature distribution of different PCM layers at the end of standby in the load-following operation (time = 2800s). Although there is no heat exchange with external, the heat conduction still occurs inside the CLHS, thus resulting in a further reduction of the temperature difference in each PCM layer.

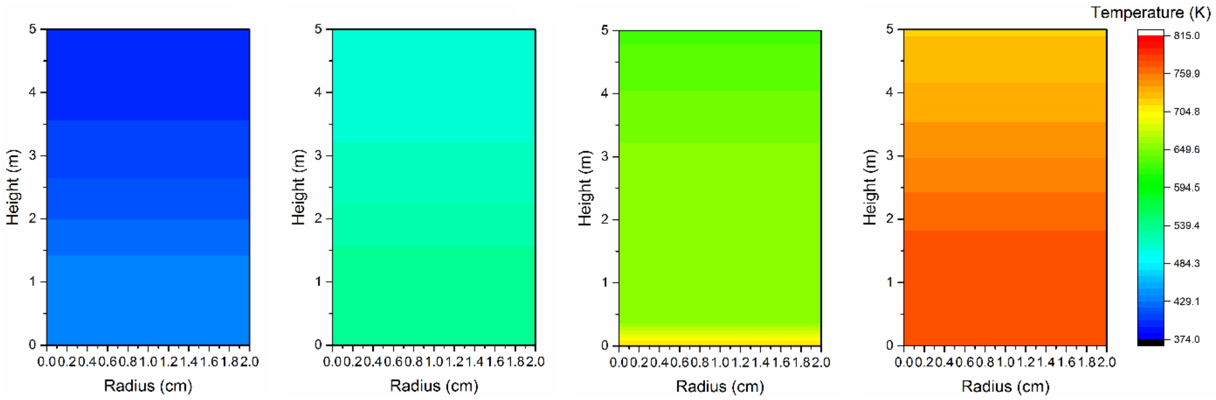

(a) PCM4 (b) PCM3 (c) PCM2 (d) PCM1

Figure 13: Temperature distribution of different PCM layers at the end of standby in the load-following operation.

4.2.3 CLHS discharging process

To meet the load demand increase from 420 MW to 428 MW, correspondingly the steam turbine output power was increased from 135 MW to 143 MW, 10 kg/s of superheated steam produced by CLHS was sent to IPTB. This is under discharging conditions, so the extracted feed water flows from the top of the CLHS to its bottom, which is the direction along the PCM melting point in ascending order. Figure 14 shows the temperature distribution of different PCM layers at the end of discharging in the load-following operation (time = 4000s). Compared to the temperature distribution of different PCM layers at the end of charging in the load-following operation (Figure 12), the radial temperature is slowly reduced from the right end to the left end at the same height of each PCM layer. This proves that an amount of heat has been transferred from the PCM layers to the feed water.

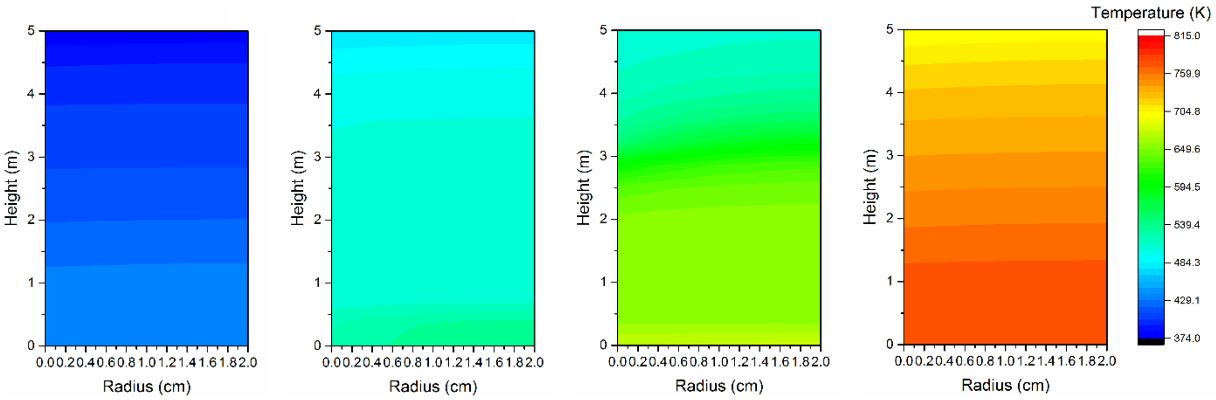

(a) PCM4 (b) PCM3 (c) PCM2 (d) PCM1

Figure 14: Temperature distribution of different PCM layers at the end of discharging in the load-following operation.

It can be seen from the simulation results that since the latent heat energy density is much higher than the sensible heat, although the temperature change is small, the amount of stored or released is large. The CLHS system with different melting temperatures can make the temperature difference between the working fluid and PCM large enough to ensure all PCMs phase changes. So that the CLHS system makes heat transfer more efficient for both charging and discharging processes.

4.2.4 Load-following dynamics

Figure 15 shows the real-time output power of the steam turbines during load-following operation. The steam turbines can correctly respond the load dynamics. Whenever the load changes, the steam turbines can respond to them within 6 mins. The response time meets the Secondary Frequency Response requirements of generating units specified in the GB Grid Code [43]. Figure 16 further reveals the amount of heat stored and released over charging and discharging during load-following operation. According to the calculation, a total of 54 GJ heat is stored in the CLHS system in the 1860 seconds and a total of 27.5 GJ heat is released to the feed water in the 1200 seconds. It can be seen that each PCM layer stores a relatively equal amount of heat during charging, but that are very different during discharging. The discharged heat from PCM4 is very small (0.1714 GJ), therefore it is not visible from the figure. This is because heat transfer is mainly determined by the heat sink (PCMs for charging and water for discharging) in both processes. During charging the local initial temperature of each PCM layer is close to its own phase change temperature and phase change occurs gradually throughout the PCM layers, so heat is stored primarily through latent heat of phase change and the thermodynamic reversibility of the process is relatively greater. However, during discharging the evaporation temperature of water does not change much, which causes its phase change to occur in only a few layers and the thermodynamic reversibility of the process is relatively smaller. This explanation can also be verified by the results shown in Figure 17. As can be seen, during charging the temperature of the exhaust gas entering and exiting each PCM layer crosses its phase change temperature (Figure 17 (a)), but during discharging only the temperature of the water entering and exiting the PCM layer 2 and 3 crosses its phase change temperature (Figure 17 (b)). Therefore, based on the different thermal properties of PCMs and water, it can be expected that there is an optimal thickness for each phase change layer to maximize the charge and discharge performance.

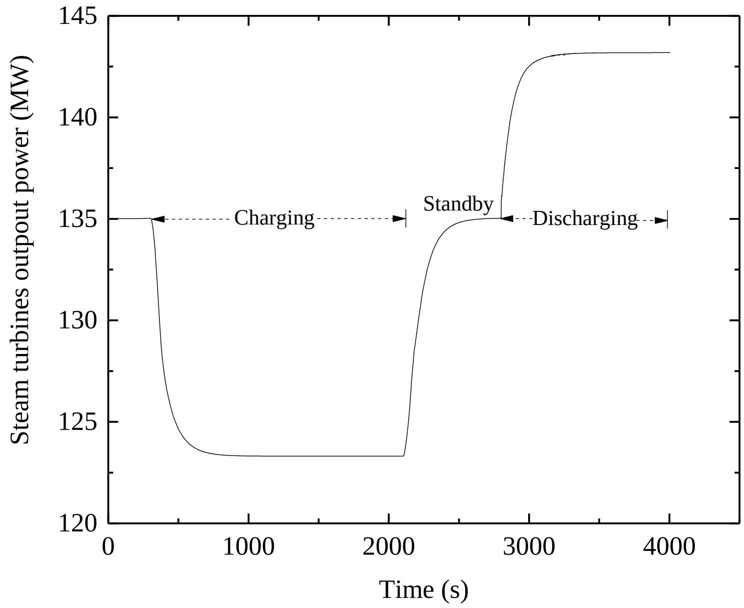

Figure 15: Real-time output power of the steam turbines during load-following operation.

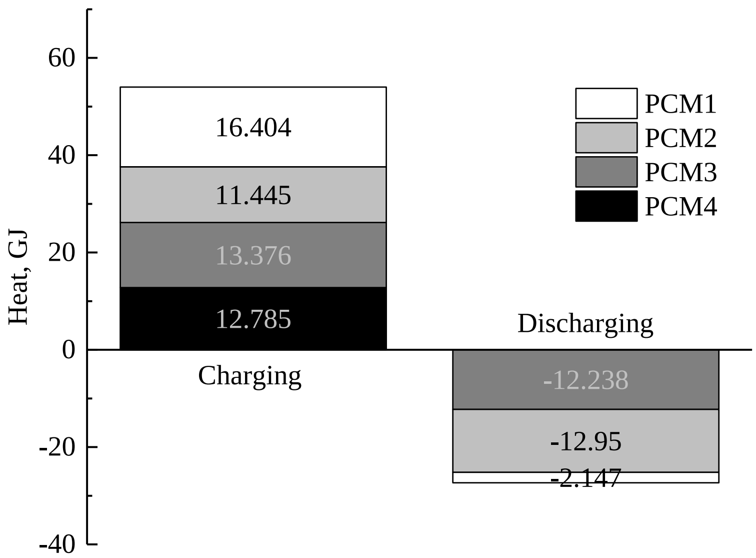

Figure 16: Amount of heat stored and released over charging and discharging during load-following operation.

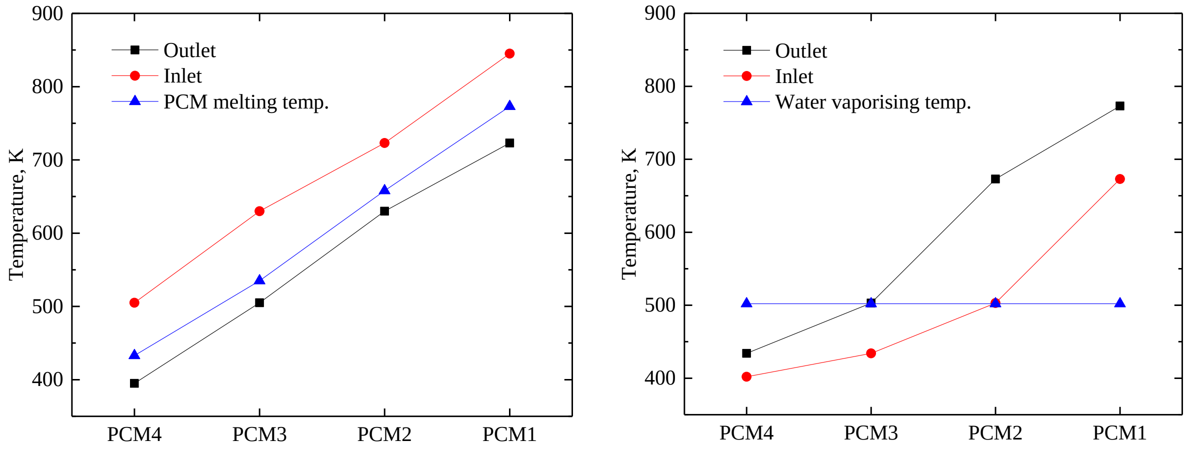

(a) (b)

Figure 17: Inlet and outlet temperature at each PCM layer at the end of charging (a) and discharging (b) during load-following operation.

4.3 CLHS *integration strategy during plant standstill*

According to the initial temperature of the material, the start-up procedure of the CCGT power plant can be divided into: hot, warm and cold start depending on the initial temperature of the material, with standstill for up to 8 hours, 48 hours and 120 hours, respectively [1]. The start-up speed is limited by the thermal stress of the steam turbine and HRSG. The longer the standstill time, the longer the start-up time is required if there is no heat preservation measure adopted. Therefore, keeping the HRSG warm is crucial vital for the CCGT power plant to restart faster. In fact, the stored thermal energy can also be used to keep HRSG warm during plant standstill period. As shown in Figure 18, during the off-load period, ambient air is fed into the CLHS to produce hot air, which is then sent to the HRSG to compensate for the heat loss of the HRSG, thereby keeping the HRSG in a hot or warm state ready for faster start-up. The potential approach is to keep the HRSG warm through the CLHS instead of maintaining the natural circulation, so the gas turbine and steam turbines can be shut down. This approach does not change the inherent structure of the HRSG and the working fluid, there should be no major technical barrier in the implementation process. In addition, the air flow rate fed into the CLHS is determined by the current temperature drop in the CLHS, and this process can be controlled by a feedback loop.

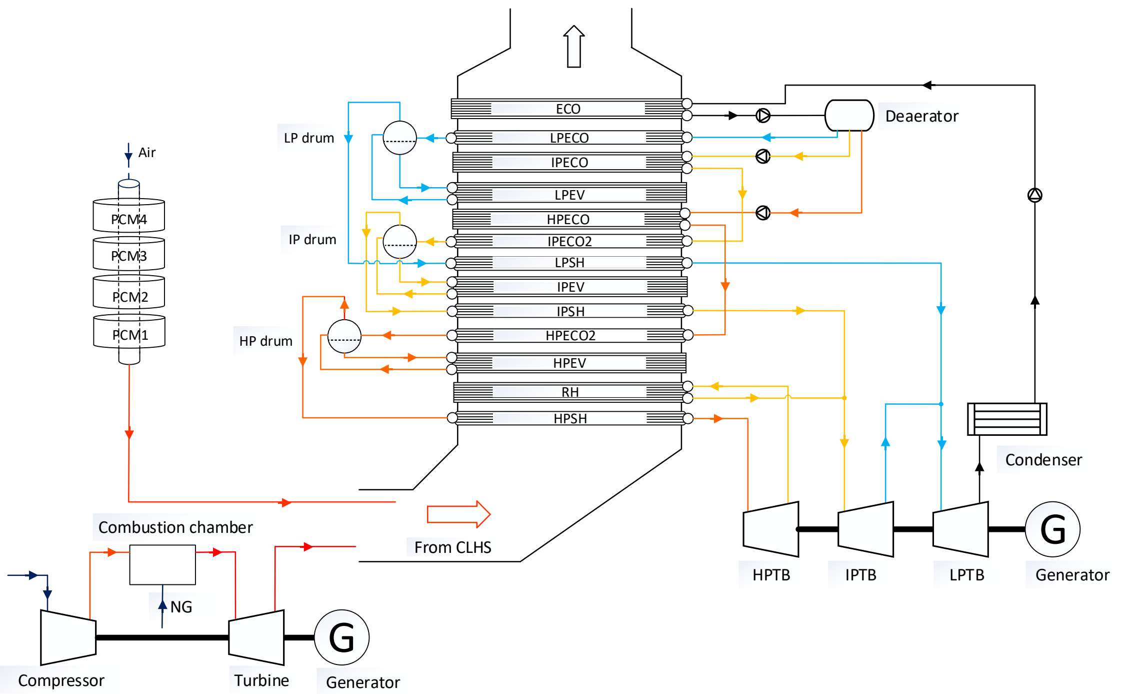

Figure 18: CLHS integration strategy for discharging during plant standstill.

5. Conclusions

This paper describes the dynamic modelling and simulation study for CLHS integration into a 420 MW CCGT power plant for flexible plant operation. A modelling method is introduced to achieve whole system dynamic simulation in Aspen Plus by an external FORTRAN code. The integration strategies during start-up, load-following and standstill operations are proposed and studied.

The dynamic simulation results shown that the strategies for CLHS integration with CCGT power plant is technically feasible. In the plant start-up processes, the gas turbine exhaust gas could pass through CLHS before discharged into atmosphere, and then the waste heat can be captured by CLHS. During the load-following operation, the output power of the CCGT power plant can be reduced by extracting exhaust gas from the gas turbine, the extracted exhaust gas is used to charge the CLHS; and the stored heat can be discharged to produce high temperature and high pressure steam for the steam turbine to increase the output power. Meanwhile the gas turbine section is still running at the rated load condition. Besides, the stored heat can also be used to maintain the HRSG under warm condition to reduce restart-up time after a standstill.

To further improve the CLHS performance under various operating models, efforts could be directed to its optimising design, such as optimising the layout of phase change materials according their thermodynamic properties, and the air flow rate used to keep the HRSG warm during a standstill.

Acknowledgements

The authors would like to acknowledge the support of the Engineering and Physical Research Council (EPSRC) for their support for the project - Flexible and Efficient Power Plant: Flex-E-Plant (Grant number: EP/K021095/1 and EP/M01536X/1) and also the grant support from EPSRC (EP/ L019469).

We also thank the following partners for their the valuable contributions: GE Energy, Doosan Babcock Limited, Centrica plc., EDF Energy (West Burton Power) Limited., Uniper Technologies Limited, Goodwin Steel Castings Limited, NPL Management Limited, R-MC Power Recovery Limited., RWE Generation UK plc., Scottish and Southern Energy (SSE) plc., Siemens Industrial Turbomachinery, and TWI Limited. The authors wish to thank the China Scholarship Council (CSC) for the PhD scholarship. The authors would like to thank the support from China Nation Basic Research Program 973 (2015CB251301).

Nomenclature

Abbreviations

CCGT	combined-cycle gas turbine
CHP	combined heat and power
ECO	economizer
HPECO	high pressure economizer
HPEV	high pressure evaporator
HPSH	high pressure superheater
HPTB	high pressure turbine
HRSG	heat recovery steam generator
IPECO	intermediate pressure economizer
IPEV	intermediate pressure evaporator
IPSH	intermediate pressure superheater
IPTB	intermediate pressure turbine
LPECO	low pressure economizer
LPEV	low pressure evaporator
LPSH	low pressure superheater
LPTB	low pressure turbine
NG	natural gas
PCM	phase change material
RH	reheater
TES	thermal energy storage

Symbols

A	Heat exchange area	m^2
c_p	Heat capacity	$J/(kg \cdot K)$
f	Weighting factor	
h	Enthalpy	J/kg
k	Heat conduction coefficient	$W/(m \cdot K)$
L	Enthalpy of phase change	$kJ \cdot kg^{-1}$
m	Mass flow rate	kg/s
$\dot{m}_t$	Ratio of mass flow rate to its designed value	
$\dot{n}_t$	Ratio of rotation speed to its designed value	
P	Pressure	Pa
Q	Heat flux of working fluid	W

r	Radius	m
t	Time	s
T	Temperature	K
T_c	Cold side temperature	K
T_h	Hot side temperature	K
ΔT	Temperature difference between hot side and cold side	K
U	Heat transfer coefficient	W/m^2K
v	Working fluid velocity	m/s
V	Volume	m^3
W	Work done on the fluid	W
W_{in}	Power input	W
$W_{in,ideal}$	Power input under ideal polytropic condition	W
W_{out}	Power output	W
$W_{out,ideal}$	Power output under ideal isentropic condition	W
z	Length	m
η_c	Compressor polytropic efficiency	
η_t	Turbine isentropic efficiency	
θ	Angle	rad
γ	Specific heat ratio	
ρ	Density	kg/m^3
<u>*Subscript*</u>		
i	Cell number	
in	Inlet stream to a process unit	
out	Outlet stream from a process unit	

References

[1] N. Mertens, F. Alobaid, T. Lanz, B. Epple, and H.-G. Kim, "Dynamic simulation of a triple-pressure combined-cycle plant: Hot start-up and shutdown," *Fuel*, vol. 167, pp. 135-148, 2016.

[2] A. Tică, H. Guéguen, D. Dumur, D. Faille, and F. Davelaar, "Design of a combined cycle power plant model for optimization," *Applied energy*, vol. 98, pp. 256-265, 2012.

[3] F. Alobaid, R. Postler, J. Ströhle, B. Epple, and H.-G. Kim, "Modeling and investigation start-up procedures of a combined cycle power plant," *Applied Energy*, vol. 85, pp. 1173-1189, 2008.

[4] A. Benato, S. Bracco, A. Stoppato, and A. Mirandola, "Dynamic simulation of combined cycle power plant cycling in the electricity market," *Energy Conversion and Management,* vol. 107, pp. 76-85, 2016.

[5] S. Afanasyeva, C. Breyer, and M. Engelhard, "The Impact of Cost Dynamics of Lithium-Ion Batteries on the Economics of Hybrid PV-Battery-GT Plants and the Consequences for Competitiveness of Coal and Natural Gas-Fired Power Plants," in *Proceedings of the 10th International Renewable Energy Storage Conference*, 2016.

[6] K. M. Powell and T. F. Edgar, "Modeling and control of a solar thermal power plant with thermal energy storage," *Chemical Engineering Science*, vol. 71, pp. 138-145, 2012.

[7] S. Kuravi, J. Trahan, D. Y. Goswami, M. M. Rahman, and E. K. Stefanakos, "Thermal energy storage technologies and systems for concentrating solar power plants," *Progress in Energy and Combustion Science,* vol. 39, pp. 285-319, 2013.

[8] S. M. Flueckiger, B. D. Iverson, S. V. Garimella, and J. E. Pacheco, "System-level simulation of a solar power tower plant with thermocline thermal energy storage," *Applied Energy,* vol. 113, pp. 86-96, 2014.

[9] T. Nuytten, B. Claessens, K. Paredis, J. Van Bael, and D. Six, "Flexibility of a combined heat and power system with thermal energy storage for district heating," *Applied energy,* vol. 104, pp. 583-591, 2013.

[10] J. D. Wojcik and J. Wang, "Technical feasibility study of thermal energy storage integration into the conventional power plant cycle," *Energies,* vol. 10, p. 205, 2017.

[11] D. Li and J. Wang, "Study of supercritical power plant integration with high temperature thermal energy storage for flexible operation," *Journal of Energy Storage,* vol. 20, pp. 140-152, 2018.

[12] N. Ceccarelli, M. van Leeuwen, T. Wolf, P. van Leeuwen, R. van der Vaart, W. Maas*, et al.*, "Flexibility of low-CO2 gas power plants: Integration of the CO2 capture unit with CCGT operation," *Energy Procedia,* vol. 63, pp. 1703-1726, 2014.

[13] Y. Hu, X. Li, H. Li, and J. Yan, "Peak and off-peak operations of the air separation unit in oxy-coal combustion power generation systems," *Applied energy,* vol. 112, pp. 747-754, 2013.

[14] Y. Hu, A. Tewari, L. Varga, H. Li, and J. Yan, "System dynamics of oxyfuel power plants with liquid oxygen energy storage," *Energy Procedia,* vol. 142, pp. 3727-3733, 2017.

[15] M. Hübel, S. Meinke, M. T. Andrén, C. Wedding, J. Nocke, C. Gierow*, et al.*, "Modelling and simulation of a coal-fired power plant for start-up optimisation," *Applied Energy,* vol. 208, pp. 319-331, 2017.

[16] Y. Zhao, C. Wang, M. Liu, D. Chong, and J. Yan, "Improving operational flexibility by regulating extraction steam of high-pressure heaters on a 660 MW supercritical coal-fired power plant: A dynamic simulation," *Applied Energy*, vol. 212, pp. 1295-1309, 2018.

[17] A. Sciacovelli, Y. Li, H. Chen, Y. Wu, J. Wang, S. Garvey*, et al.*, "Dynamic simulation of Adiabatic Compressed Air Energy Storage (A-CAES) plant with integrated thermal storage–Link between components performance and plant performance," *Applied energy,* vol. 185, pp. 16-28, 2017.

[18] E. Pihl, S. Heyne, H. Thunman, and F. Johnsson, "Highly efficient electricity generation from biomass by integration and hybridization with combined cycle gas turbine (CCGT) plants for natural gas," *Energy,* vol. 35, pp. 4042-4052, 2010.

[19] R. Canepa and M. Wang, "Techno-economic analysis of a CO_2 capture plant integrated with a commercial scale combined cycle gas turbine (CCGT) power plant," *Applied Thermal Engineering,* vol. 74, pp. 10-19, 2015.

[20] A. Mathisen, H. Sørensen, M. C. Melaaen, and G.-I. Müller, "Investigation into optimal CO_2 concentration for CO_2 capture from aluminium production," 2013.

[21] J. François, L. Abdelouahed, G. Mauviel, M. Feidt, C. Rogaume, O. Mirgaux*, et al.*, "Estimation of the energy efficiency of a wood gasification CHP plant using Aspen Plus," *Chem. Eng. Trans,* vol. 29, pp. 769-774, 2012.

[22] T. Adams and N. Mac Dowell, "Off-design point modelling of a 420MW CCGT power plant integrated with an amine-based post-combustion CO_2 capture and compression process," *Applied Energy,* vol. 178, pp. 681-702, 2016.

[23] P. M. Mathias, H. C. Klotz, and J. M. Prausnitz, "Equation-of-state mixing rules for multicomponent mixtures: the problem of invariance," *Fluid Phase Equilibria,* vol. 67, pp. 31-44, 1991.

[24] W. Wagner and A. Pruß, "The IAPWS formulation 1995 for the thermodynamic properties of ordinary water substance for general and scientific use," *Journal of physical and chemical reference data,* vol. 31, pp. 387-535, 2002.

[25] S. M. H. Mahmood, M. G. Turner, and K. Siddappaji, "Flow characteristics of an optimized axial compressor rotor using smooth design parameters," in *ASME Turbo Expo 2016: Turbomachinery Technical Conference and Exposition*, 2016, pp. V02CT45A018-V02CT45A018.

[26] M. Ameri, P. Ahmadi, and S. Khanmohammadi, "Exergy analysis of a 420 MW combined cycle power plant," *International Journal of Energy Research,* vol. 32, pp. 175-183, 2008.

[27] M. T. Mansouri, P. Ahmadi, A. G. Kaviri, and M. N. M. Jaafar, "Exergetic and economic evaluation of the effect of HRSG configurations on the performance of combined cycle power plants," *Energy Conversion and Management,* vol. 58, pp. 47-58, 2012.

[28] N. Zhang and R. Cai, "Analytical solutions and typical characteristics of part-load performances of single shaft gas turbine and its cogeneration," *Energy Conversion and Management,* vol. 43, pp. 1323-1337, 2002.

[29] S. Quoilin, R. Aumann, A. Grill, A. Schuster, V. Lemort, and H. Spliethoff, "Dynamic modeling and optimal control strategy of waste heat recovery Organic Rankine Cycles," *Applied Energy,* vol. 88, pp. 2183-2190, 2011.

[30] B. Tashtoush, M. Molhim, and M. Al-Rousan, "Dynamic model of an HVAC system for control analysis," *Energy,* vol. 30, pp. 1729-1745, 2005.

[31] D. Li, Y. Hu, W. He, and J. Wang, "Dynamic modelling and simulation of a combined-cycle power plant integration with thermal energy storage," in *Automation and Computing (ICAC), 2017 23rd International Conference on*, 2017, pp. 1-6.

[32] F. Agyenim, N. Hewitt, P. Eames, and M. Smyth, "A review of materials, heat transfer and phase change problem formulation for latent heat thermal energy storage systems (LHTESS)," *Renewable and sustainable energy reviews,* vol. 14, pp. 615-628, 2010.

[33] W. Zhao, D. M. France, W. Yu, T. Kim, and D. Singh, "Phase change material with graphite foam for applications in high-temperature latent heat storage systems of concentrated solar power plants," *Renewable Energy,* vol. 69, pp. 134-146, 2014.

[34] K. Lafdi, O. Mesalhy, and A. Elgafy, "Graphite foams infiltrated with phase change materials as alternative materials for space and terrestrial thermal energy storage applications," *Carbon,* vol. 46, pp. 159-168, 2008.

[35] B. Cárdenas and N. León, "High temperature latent heat thermal energy storage: Phase change materials, design considerations and performance enhancement techniques," *Renewable and sustainable energy reviews,* vol. 27, pp. 724-737, 2013.

[36] M. M. Kenisarin, "High-temperature phase change materials for thermal energy storage," *Renewable and Sustainable Energy Reviews,* vol. 14, pp. 955-970, 2010.

[37] S. Patankar, *Numerical Heat Transfer and Fluid Flow*: McGraw Hill, 1980.

[38] P. Verma and S. Singal, "Review of mathematical modeling on latent heat thermal energy storage systems using phase-change material," *Renewable and Sustainable Energy Reviews,* vol. 12, pp. 999-1031, 2008.

[39] A. Gil, M. Medrano, I. Martorell, A. Lázaro, P. Dolado, B. Zalba*, et al.*, "State of the art on high temperature thermal energy storage for power generation. Part 1—Concepts, materials and modellization," *Renewable and Sustainable Energy Reviews,* vol. 14, pp. 31-55, 2010.

[40] F. Alobaid, S. Pfeiffer, B. Epple, C.-Y. Seon, and H.-G. Kim, "Fast start-up analyses for Benson heat recovery steam generator," *Energy,* vol. 46, pp. 295-309, 2012.

[41] A. Pasha, "Combined cycle power plant start-up effects and constraints of the HRSG," in *ASME 1992 International Gas Turbine and Aeroengine Congress and Exposition*, 1992, pp. V004T11A016-V004T11A016.

[42] T. Kim, D. Lee, and S. Ro, "Analysis of thermal stress evolution in the steam drum during start-up of a heat recovery steam generator," *Applied Thermal Engineering,* vol. 20, pp. 977-992, 2000.

[43] X. Luo, J. Wang, J. D. Wojcik, J. Wang, D. Li, M. Draganescu*, et al.*, "Review of Voltage and Frequency Grid Code Specifications for Electrical Energy Storage Applications," *Energies,* vol. 11, pp. 1-26, 2018.